Symmetry-Breaking-Induced Multifunctionalities of Two-Dimensional Chromium-Based Materials for Nanoelectronics and Clean Energy Conversion

Lei Li,[1] Tao Huang,[1] Kun Liang,[1] Yuan Si,[1] Ji-Chun Lian,[1] Wei-Qing Huang,[1,*] Wangyu Hu,[2] and Gui-Fang Huang[1,†]

[1] *Department of Applied Physics, School of Physics and Electronics, Hunan University, Changsha 410082, China*
[2] *School of Materials Science and Engineering, Hunan University, Changsha 410082, China*

(Received 13 January 2022; revised 11 June 2022; accepted 16 June 2022; published 7 July 2022)

Structural symmetry breaking, which could lead to exotic physical properties, plays a crucial role in determining the functions of a system, especially for two-dimensional (2D) materials. Here, we demonstrate that multiple functionalities of 2D chromium-based materials can be achieved by breaking inversion symmetry via replacing Y atoms in one face of pristine CrY (Y = P, As, Sb) monolayers with N atoms, i.e., forming Janus Cr_2NY monolayers. The functionalities include gapless spin, very low work function, inducing carrier doping, and catalytic activity, which are predominately ascribed to the large intrinsic dipole of Janus Cr_2NY monolayers, giving them great potential for various applications. Specifically, Cr_2NSb is found to be a spin-gapless semiconductor, Cr_2NP and Cr_2NHPF can simultaneously induce n- and p-type carrier doping for two graphene sheets with different concentrations (forming an intrinsic p-n vertical junction), and Cr_2NY exhibits excellent electrocatalytic hydrogen-evolution activity, even superior to that of benchmark Pt. The results confirm that breaking symmetry is a promising approach for the rational design of multifunctional 2D materials.

DOI: 10.1103/PhysRevApplied.18.014013

I. INTRODUCTION

Symmetry principles that play an important role with respect to the laws of nature are universally used by the scientific community and can simplify the solution of problems, thus easily disclosing key conclusions. When breaking the symmetry of a system, bizarre physical properties, such as plasmonic exceptional points and the valley Hall effect, can appear [1–5]. The past few years have witnessed the rapid development of symmetry-breaking two-dimensional (2D) materials. Notably, Janus transition-metal dichalcogenides (TMDs) have become the focus and frontier of 2D materials with mirror-symmetry breaking, because their three-atom-layer structure naturally possesses the possibility to intrinsically break the out-of-plane mirror symmetry [6]. Experimentally, a semiconducting Janus MoSSe with one face consisting of Se atoms and the other of S atoms was synthesized in 2017 independently by Lu *et al.* [7] and by Zhang *et al.* [8]. This breakthrough has inspired a surge of theoretical and experimental research into Janus 2D materials, including but not limited to MoSSe, which exhibit unique physical and chemical properties different from their symmetrical counterparts. For instance, a long exciton radiative recombination lifetime is found in Janus MoSSe and WSSe monolayers [9], and considerable spin Hall conductivities [10], efficient water-splitting performance [11], and tunable electronic and electron transport properties [12] are predicted in Janus MoSSe. Due to their unique structure and properties, Janus 2D materials show great potential for applications in nanoelectronics (such as valleytronics [13] and gas sensing [14]) and clean energy conversion (such as photovoltaics [15,16] and water splitting [17,18]).

Recently, 2D chromium-based materials have received great attention due to their unique structural topology and intrinsic magnetic properties [19–26]. For example, the CrN monolayer is predicted to be a planar one-atomic-layer-thick structure with robust ferromagnetism [19] or an almost flat hexagonal sheet with minor buckling due to the reduction of a surface dipole moment [20,21]. Similarly, hexagonal monolayers of chromium pnictides CrX (X = P, As, Sb, Bi) are found to be one-atomic-layer-thick flat structures (zero buckling between Cr and X atoms) and ferromagnetically ordered systems with Curie temperatures well above 300 K [22]. At the same time, two-atomic-layer-thick structural CrX (X = P, As monolayers are also theoretically demonstrated [23]. As the most well-known case of 2D Cr-based materials, the CrI_3 monolayer is a three-atomic-layer-thick structure, analogous to TMDs, and ferromagnetic (FM) order can be observed at

*wqhuang@hnu.edu.cn
†gfhuang@hnu.edu.cn

temperatures below 45 K when few layers are stacking [26]. This finding has provoked a number of experimental and theoretical investigations to try to control the magnetism and realize field-effect devices based on CrI_3 multilayers [27–34]. Both the diversity of structural topology and eccentric properties revealed by these works demonstrate that 2D Cr-based materials are an interesting platform, even surpassing 2D TMDs, to study the fundamental physics of 2D materials and have exciting application potential in various fields. Although some progress has been made in 2D Cr-based materials, related studies and knowledge are still in their infancy.

Herein, we report a family of 2D Cr-based materials—three-atomic-layer-thick CrY (Y = P, As, Sb) monolayers and their Janus counterparts, Cr_2XY (X = P, As, Sb) and Cr_2NY. We find that breaking the symmetry (i.e., using N atoms to substitute Y atoms on one side) of pristine CrY monolayers will induce a large out-of-plane intrinsic dipole owing to the electronegativity of the N atom being much larger than that of Y atoms and its related multifunctionalities. Interestingly, the Cr_2NSb monolayer is found to be a spin-gapless semiconductor, and functionalizing Cr_2NP can increase the dipole moment and greatly lower the work function to 2.46 eV. When the Cr_2NP or Cr_2NHPF monolayer is sandwiched between two graphene sheets, an interfacial interaction will induce carrier doping in two graphene sheets with different concentrations, thus forming an intrinsic p-n vertical junction. Moreover, Janus Cr_2NY monolayers exhibit excellent electrocatalytic hydrogen-evolution activity at N-atom sites, even superior to that of benchmark Pt. The amazing properties of 2D Cr-based materials lead to exciting applications in nanoelectronics and clean energy conversion.

II. COMPUTATIONAL METHOD

All the calculations are performed using the first-principles theory within the framework of density-functional theory (DFT) as implemented in the Vienna *ab initio* simulation package [35,36]. The projector augmented wave potentials are utilized to deal with the interaction between core electrons [37]. The generalized gradient approximation (GGA) given by Perdew-Burke-Ernzerhof (PBE) is adopted for exchange-correlation functionals [38]. The spin-dependent GGA plus Hubbard U (GGA + U) approximately describes the strongly correlated interactions of the transition metal Cr, where the Hubbard U parameter of the Cr atom is set to 3.0 eV [39,40]. The screened hybrid Heyd-Scuseria-Ernzerhof (HSE06) functional without Hubbard U correction is used for the calculations of more reliable band gaps [41,42]. The plane-wave cutoff energy is set to 550 eV, and atomic coordinates are fully relaxed to ensure the total energy in 10^{-5} eV precision and force in 10^{-2} eV Å^{-1} convergence. The k points with a $7 \times 7 \times 1$ grid for structure relaxation, and a $9 \times 9 \times 1$ grid for the self-consistent field calculations, are sampled by the gamma-centered Monkhorst-Pack grids. To eliminate the coupling force between the periodic images, a vacuum space of 20 Å is inserted along the z direction for the monolayers and 30 Å for the heterostructures. The van der Waals (vdW) interaction between the monolayers and graphene or H atom are described by the DFT-D3 method [43]. The phonon calculations are carried out by using DFT perturbation theory, as implemented in the PHONOPY code [44–46]. A $3 \times 3 \times 1$ supercell is adopted to construct the dynamic matrix and calculate the phonon dispersion. Note that the dipole correction has an ignorable impact on the electronic structures and application properties of the monolayers; thus, we do not consider the dipole correction in the following calculations, except the calculation of the dipole moment and electrostatic potential.

III. RESULTS AND DISCUSSION

A. The geometric structures and electronic properties

Symmetry is essential to science. To explore the effect of symmetry breaking, we first study symmetrical CrY (Y = P, As, Sb) monolayers that all belong to space group *Pnmm* with 2D networks of rectangular sublattices in the x-y plane. Figure 1(a) displays top and side views of CrY monolayers, where the Cr atoms are sandwiched between Y atoms on both sides, showing symmetrical structures. In view of the exotic properties of Janus monolayers because of breaking structural symmetry, Y atoms on one side of CrY monolayers are replaced with X atoms to obtain Janus Cr_2XY (X, Y = P, As, Sb), as shown in Fig. 1(b), wherein the atomic radius of X atoms is smaller than that of Y atoms. Similarly, Cr_2NY (Y = P, As, Sb) monolayers shown in Fig. 1(c) are obtained by substituting N atoms. Table I lists the optimized lattice constants and bond lengths. For CrY monolayers, the Y—Cr bond length decreases with an increase in the electronegativity of the Y atom. Accordingly, the optimized lattice constant of CrY with a longer Y—Cr bond is bigger; the bond lengths are 4.173, 4.262, and 4.396 Å for CrP, CrAs, and CrSb, respectively. For Cr_2XY cases, the P—Cr, As—Cr, and Sb—Cr bond lengths are almost equal to those in the CrY monolayers, and the optimized lattice constants are between those of CrX and CrY. But for Cr_2NY cases, due to much greater electronegativity of the N atom, the N—Cr bonds are much shorter than the P—Cr bond, thus the optimized lattice constants of the Cr_2NY monolayer are smaller than all of the CrY ones.

Formation-energy (E_f) calculations are performed to investigate the energetic stability with

$$E_f = E_{\text{total}} - \sum_{i=1}^{4} E_i,$$

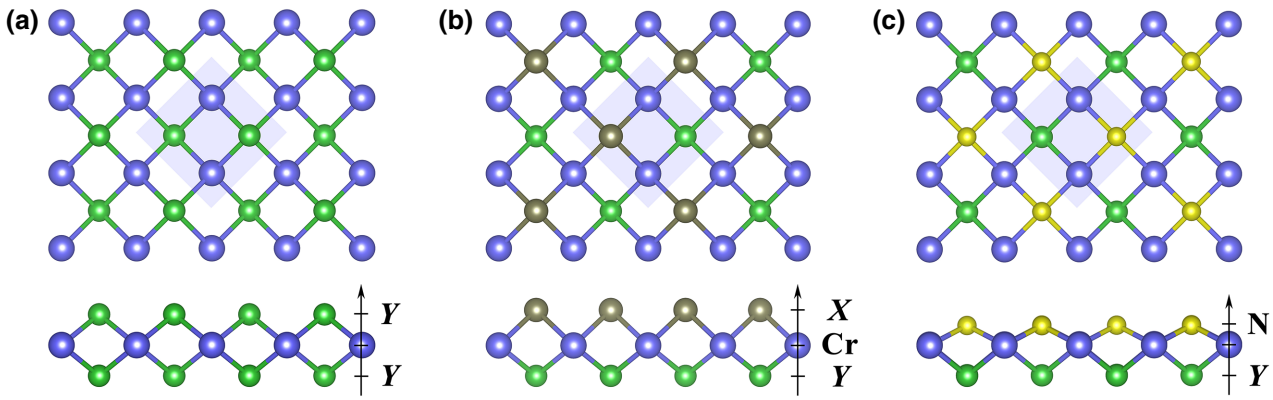

FIG. 1. Top (top panels) and side (lower panels) views of (a) CrY, (b) Cr_2XY, and (c) Cr_2NY monolayers (X, Y = P, As, Sb). Blue regions represent the unit cells; yellow, green, brown, and blue balls represent N, Y, X, and Cr, respectively.

where E_{total} represents the total cell energy; E_i refers to the chemical potential of each atom of the unit cell, which is the normalized energy of the corresponding bulk phase. It can be seen from Table SI within the Supplemental Material [47] that the formation energies of the monolayers have negative values, showing energetic stability. At the same time, we note that CrY is proposed to have a stable 2D hexagonal structure (h-CrY). To compare their energies, we calculate the formation enthalpy (ΔH) of each CrY based on the energy differences between the tetragonal (4 atoms in each cell) and hexagonal (2 atoms in each cell) lattices:

$$\Delta H(\text{Cr}Y) = E_{\text{Cr}Y} - 2E_{h\text{-Cr}Y}.$$

As shown in Table SI within the Supplemental Material [47], the calculated negative values prove that tetragonal CrY are more stable in energy. For the constructed Janus monolayers, it is essential to compare the stability with symmetric CrY. Here, we calculate $\Delta H(\text{Cr}_2XY)$ based on tetragonal CrY, which are more stable than h-CrY:

$$\Delta H(\text{Cr}_2XY) = E_{\text{Cr}_2XY} - \frac{1}{2}E_{\text{Cr}X} - \frac{1}{2}E_{\text{Cr}Y}.$$

Negative values (Table SI within the Supplemental Material [47]) suggest that the formation of Janus Cr_2XY from CrY is an exothermic process, and their decomposition into symmetrical CrY requires overcoming barriers. For Cr_2NY, the CrN tetragonal lattice has a large virtual frequency, but the hexagonal lattice structure (h-CrN) proves to be stable. Therefore, based on h-CrN, we calculate the formation enthalpies of Cr_2NY as:

$$\Delta H(\text{Cr}_2\text{N}Y) = E_{\text{Cr}_2\text{N}Y} - E_{h\text{-CrN}} - \frac{1}{2}E_{\text{Cr}Y}.$$

Interestingly, the formation enthalpy of each Cr_2NY is smaller than that of Cr_2XY, indicating that the decomposition of each Cr_2NY structure into symmetric monolayer requires a larger barrier to be overcome.

To determine dynamic stability, the phonon dispersion is calculated and shown in Fig. S1 within the Supplemental Material [47], which includes three acoustic and nine optical branches corresponding to four atoms in each unit cell for every structure, and the phonon modes are free from any imaginary frequencies throughout the whole Brillouin zone (BZ), indicating the intrinsic structural stability of CrY, Cr_2XY, and Cr_2NY monolayers. However, the CrN

TABLE I. Optimized lattice constants (a), bond lengths (d), dipole moments (μ), exchange energies ($E_{\text{AFM-FM}}$), and band gaps determined by GGA + U ($E_g^{\text{GGA}+U}$) and HSE06 (E_g^{HSE06}) of CrX, Cr_2XY, and Cr_2NY monolayers.

Monolayer	a (Å)	$d_{X\text{—Cr}}$ (Å)	$d_{Y\text{—Cr}}$ (Å)	μ (D)	$E_{\text{AFM-FM}}$ (meV)	$E_g^{\text{GGA}+U}$ (eV)	E_g^{HSE06} (eV)
CrP	4.173		2.409	0	700.8	0.041	0.543
CrAs	4.262		2.528	0	676.6	0.067	0.437
CrSb	4.396		2.752	0	497.7	0	0
Cr_2PAs	4.216	2.406	2.532	0.05	676.1	0.145	0.607
Cr_2PSb	4.289	2.400	2.757	0.12	480.2	0.126	0.514
Cr_2AsSb	4.329	2.522	2.757	0.09	522.6	0	0.140
Cr_2NP	3.873	2.005	2.406	0.39	839.9	0.081	0.818
Cr_2NAs	3.913	2.010	2.529	0.33	427.4	0	0.872
Cr_2NSb	3.942	2.005	2.768	0.26	62.08	0	0.001

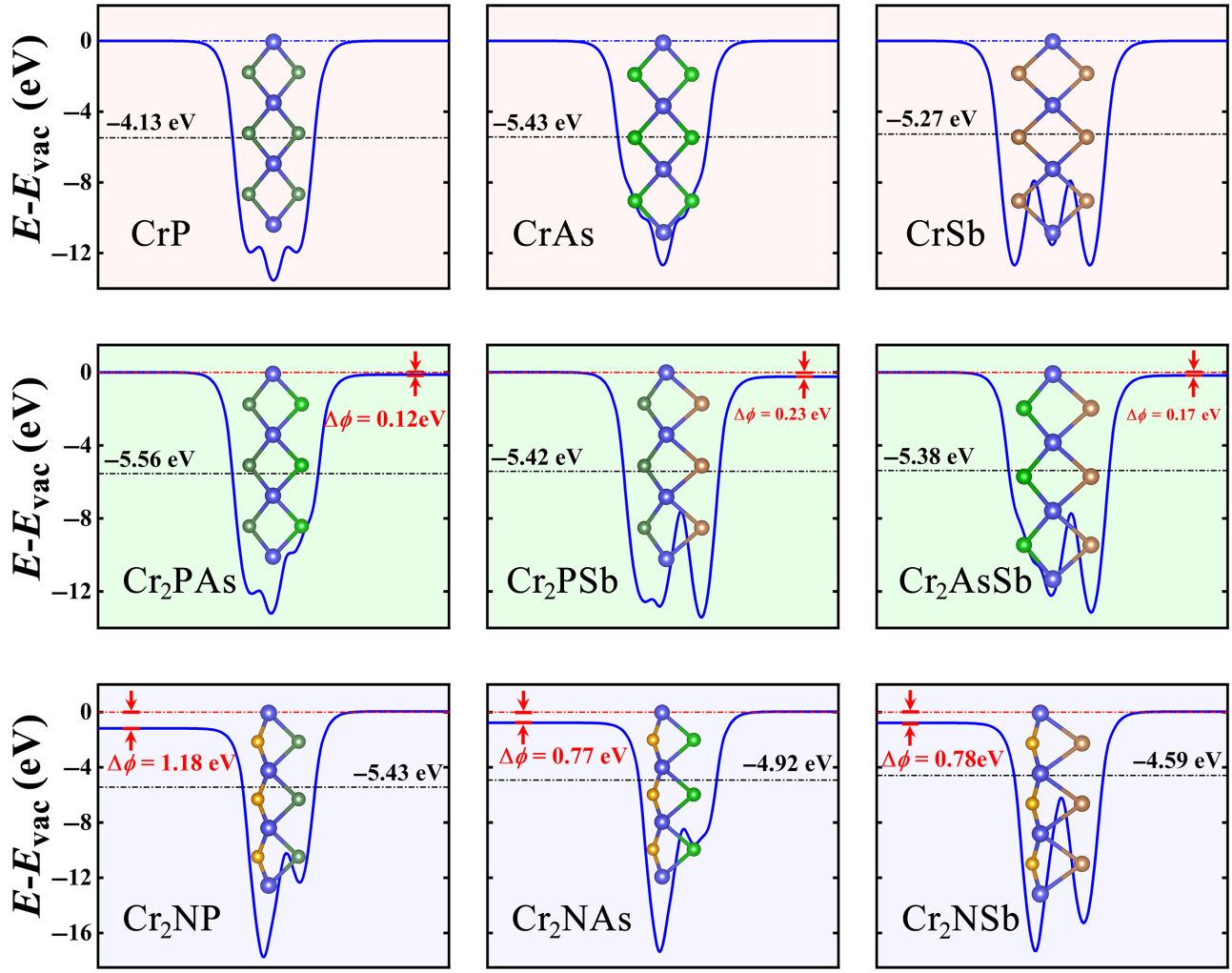

FIG. 2. Electrostatic potential with respect to the vacuum energy in the direction perpendicular to CrY, Cr_2XY, and Cr_2NY monolayers. Red and black energy values are electrostatic potential differences and Fermi level, respectively; yellow, dark green, green, brown, and blue balls in the structures represent N, P, As, Sb, and Cr, respectively.

monolayer is found to be unstable [Fig. S2(a) within the Supplemental Material [47]]. It is also necessary to assess the effect of lattice distortion on structural stability. To guarantee the positive definiteness of strain energy following lattice distortion, the linear elastic constants of a stable crystal have to obey the Born-Huang criteria. For a mechanically stable 2D monolayer with tetragonal symmetry, the elastic constants need to satisfy $C_{11} > |C_{12}|$ and $C_{66} > 0$. We calculate the elastic constants of CrY, Cr_2XY, and Cr_2NY monolayers and find that, except for Cr_2AsSb (the Cr_2AsSb monolayer is not focused below), the monolayers can satisfy the conditions (Table SI within the Supplemental Material [47]), indicating that the monolayers, except Cr_2AsSb, are mechanically stable. Due to the great prospects for Janus monolayers, a further stability calculation is needed, especially for Janus monolayers with a large dipole. Here, the thermal stability of the Cr_2NP and Cr_2NAs lattices (which are shown below to possess larger dipoles) is assessed by performing *ab initio* molecular dynamics (AIMD) simulations. Snapshots at 0 and 5000 fs, plotted in Fig. S3 within the Supplemental Material [47], show that there is almost no phase transition within 5 ps for the 2D planar networks, suggesting that Cr_2NY are thermally stable at 300 K. The time-dependent evolutions of total energies show a small fluctuation, further confirming the thermal stability.

Structural symmetry breaking can significantly influence the physical properties of 2D materials [4,5]. To testify to this, the dipole moments of all monolayers are calculated and listed in Table I. In Janus Cr_2XY monolayers, Cr atoms are coordinated with X and Y atoms, forming trigonal prisms with mirror asymmetry, leading to a dipole pointing from Y to X atoms; the dipole moments are 0.05, 0.12, and 0.09 D for Cr_2PAs, Cr_2PSb, and Cr_2AsSb, respectively (the dipole disappears in symmetrical CrY monolayers). Things are more interesting in Cr_2NY

monolayers that have a greater electronegativity difference between N and Y atoms, resulting in larger dipole moments; these are 0.39, 0.33, and 0.26 D for Cr_2NP, Cr_2NAs, and Cr_2NSb, respectively. Therefore, breaking the symmetry by substituting N atoms can effectively increase the dipole moment, especially for Cr_2NP, which is more than 2 times that of MoSSe (0.18 D) [48,49].

Generally, the dipole of 2D Janus monolayers, such as MoSSe, points from one side of the atom with lower electronegativity to the other side, and things are the same in Cr_2XY. Unexpectedly, the opposite situation is found in Cr_2NY monolayers, where the dipole points from N to Y atoms, where the Y atom possesses a lower electronegativity than that of the N atom. This anomalous behavior in Cr_2NY can be proved as follows. The net vertical electric field generated from the dipole can induce a difference in electrostatic potential on both sides of the Janus monolayers, and the side with higher potential is always the end where the dipole points to. Thus, to further verify the size and direction of the dipole, we can investigate electrostatic potentials in the direction perpendicular to the monolayers, as shown in Fig. 2. For CrY monolayers, it aligns with the vacuum energy at both ends because there is no dipole in these symmetrical structures. For Cr_2XY monolayers, the potentials are 0.12, 0.23, and 0.17 eV lower at the Y sides of Cr_2PAs, Cr_2PSb, and Cr_2AsSb, respectively, where Y atoms possess lower electronegativity. Whereas, in each Cr_2NY monolayer, the side of the N atoms, which possesses higher electronegativity, has a lower potential than the other side, where the potential differences are 1.18, 0.77, and 0.78 eV for Cr_2NP, Cr_2NAs, and Cr_2NAs, respectively.

To explain the above phenomenon, we propose a simplified model to analyze the local dipole. The intrinsic dipoles can be directly calculated, but it is difficult to deal with the local dipole. A solution is to divide the three-atom-layer structure into two parts, from Cr to atoms on both sides (Fig. 3), and then the local dipoles can be roughly solved by Bader charges and atomic layer spacings between Cr and one of the sides, which can be used to determine the root of the larger dipole with an abnormal direction for Cr_2NY. Here, the two local dipoles can be written as

$$\mu_i = \Delta q_i \Delta z_i; (i = 1, 2),$$

where μ_i, Δq_i, and Δz_i are the local dipole moments, Bader charges, and atomic layer spacings along the z direction between Cr and one of the sides, respectively; these are calculated and summarized in Table SII within the Supplemental Material [47]. For CrY, μ_1 and μ_2 have equal values but opposite directions, because identical Y atoms lead to equal charge transfer (Δq_1 and Δq_2) and equal spacing (Δz_1 and Δz_2) between Cr and Y on both sides. Figure 3(a) shows the results for the CrP monolayer, indicating there is no dipole, and the situation is the same for CrAs and

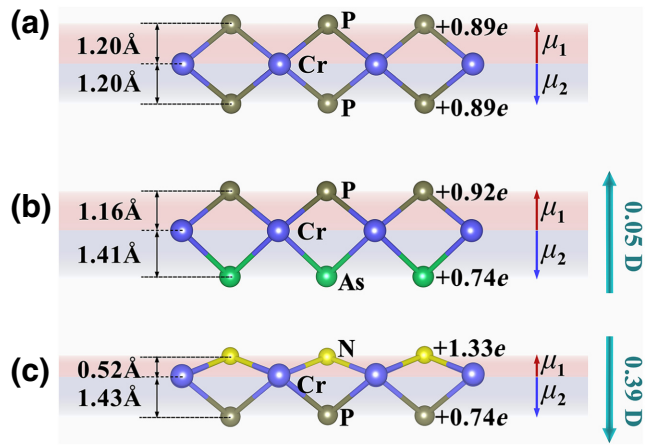

FIG. 3. Dipole schematic diagram of (a) CrP, (b) Cr_2PAs, and (c) Cr_2NP monolayers. Pink and purple regions show local dipoles with different directions; black numbers show transferred charge and spacing along the z direction on both sides; green arrows and numbers show actual dipole moments.

CrSb. On the contrary, for Cr_2XY and Cr_2NY monolayers, charge transfer and atomic layer spacings from Cr to the two sides are different due to their different electronegativities, leading to different μ_1 and μ_2, where μ_1 (μ_2) can be defined as pointing to atoms with higher (lower) electronegativity. For Cr_2XY monolayers, the local dipole μ_1 has a bigger value than μ_1 because of the larger Δq_1, leading to the direction of the dipole from Y to X atoms. Note that the actual intrinsic dipole, μ, in Cr_2XY monolayers is small owing to the small differences of charge transfer and atomic layer spacing on both sides; The Cr_2PAs monolayer is taken as an example and shown in Fig. 3(b). For Cr_2NY monolayers, however, the atomic layer spacing, Δz_1 (Cr-N), is much shorter than Δz_2 (Cr-Y), thus the local dipole μ_1 is much smaller than μ_2. As a result, the intrinsic dipole, μ, in Cr_2NY monolayers is large and points from N to Y atoms. For example, focusing on Cr_2NP [Fig. 3(c)], although charge transfer Δq_1 is nearly twice as large as Δq_2, atomic layer spacing Δz_1 is about a third shorter than Δz_2, resulting in local dipole μ_1 being much smaller than μ_2. Therefore, Cr_2NY monolayers have a large dipole with the opposite direction; this relies on electronegativity differences between N and Y atoms. Furthermore, we compare the calculated total dipole moments (μ) with the local dipole moments differences (μ_1–μ_2), where negative values of μ represent an abnormal direction. The results (Fig. S4 within the Supplemental Material [47]) show that they fit well, especially for Cr_2PAs, Cr_2NP, and Cr_2NAs. For the structures containing the Sb atom, the local dipole differences give higher values because the electronegativity of Sb is similar to that of Cr, but very different from that of the nonmetallic atom (N, P or As), which means that the local dipole between Sb and the nonmetallic atom cannot be ignored, leading to a slight error. However, the

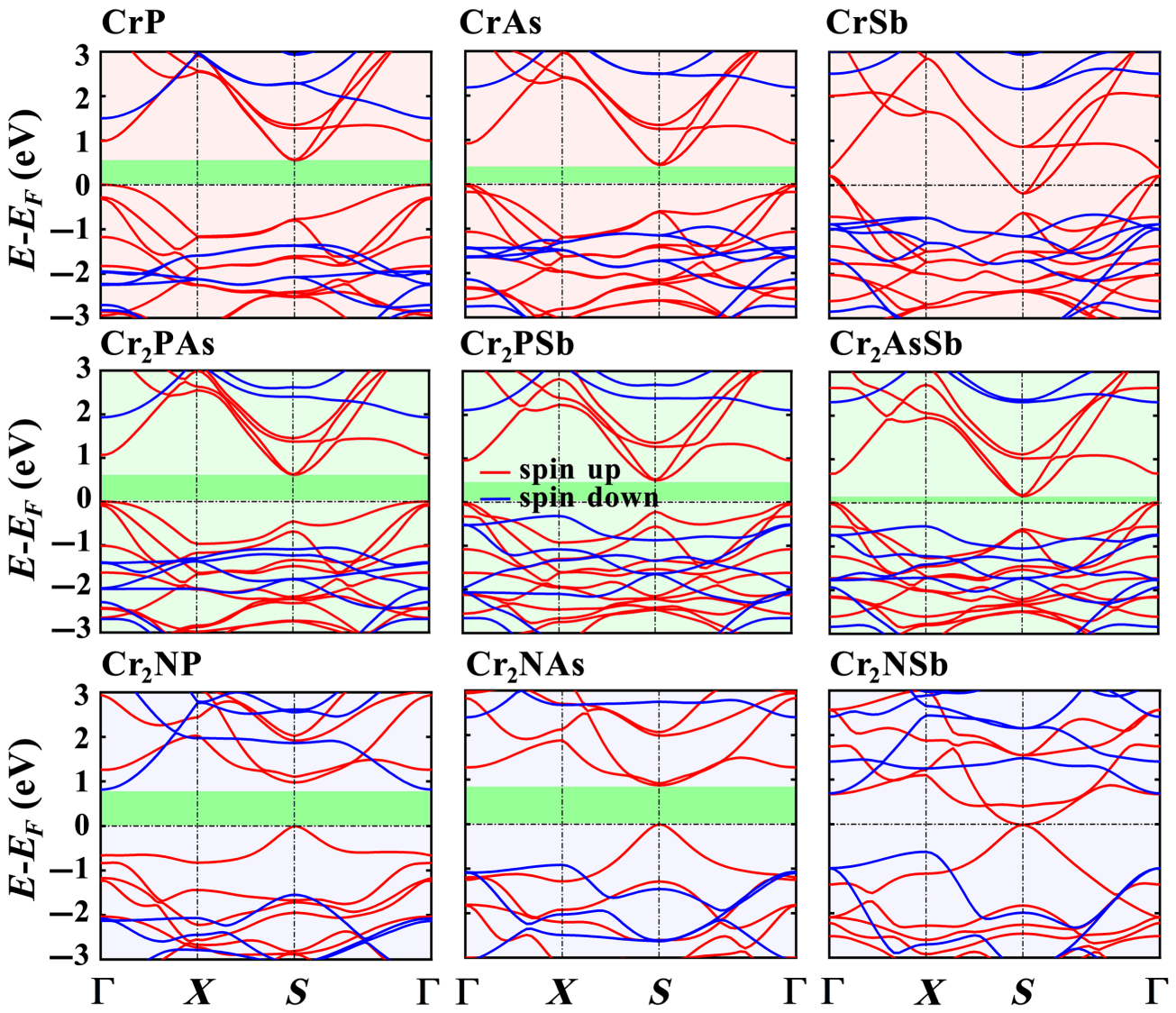

FIG. 4. Spin-polarized electronic band structures calculated with the HSE functional with respect to E_F of the CrY, Cr_2XY, and Cr_2NY monolayers. Red and blue lines represent bands projected to spin up and spin down; energy gap is highlighted in green.

local-dipole model still gives similar values and a direction consistent with μ. Therefore, it is feasible to analyze the dipole of Cr_2NY with the local-dipole model.

To determine the magnetic ground state, we carry out calculations of the energy differences ($E_{\mathrm{AFM-FM}}$) between FM and antiferromagnetic (AFM) states, where the AFM state is briefly set to the opposite spin direction for Cr atoms in the unit cell. The positive values of $E_{\mathrm{AFM-FM}}$ (Table I) reveal the FM ground states for all CrY, Cr_2XY, and Cr_2NY monolayers. In the monolayers, each Cr atom gives three electrons to form ionic bonds with the ligands and leaves three electrons, so there is a large magnetic moment of 6 μ_B in each unit cell.

As listed in Table I, the band-gap energies calculated by the GGA + U method are lower than those obtained with the HSE06 hybrid-functional method, because the independent electron picture breaks down as a result of strong Coulombic interactions [50–52]. To investigate the electronic properties of the FM ground states of these monolayers, we focus on the spin-polarized electronic band structures calculated by the HSE06 hybrid-functional method. According to the characteristics of the structures, we choose the high-symmetry k path in the Brillouin zone, as shown in Fig. S2(b) within the Supplemental Material [47]. Figure 4 shows the bands projected onto spin-up and spin-down directions represented by red and blue lines, respectively. For CrY monolayers (top part in Fig. 4), it is found that the band of the CrSb monolayer is metallic, but the CrP and CrAs ones are semiconductors with indirect gaps of 0.543 and 0.437 eV, respectively, the valence-band maximum (VBM) and conduction-band minimum (CBM) edges of which are located at the Γ and S points of the BZ,

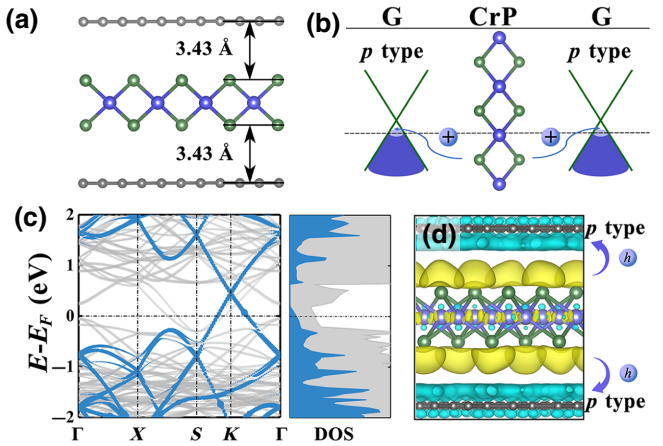

FIG. 5. (a) Structure of vdW heterostructure G/CrP/G. Numbers indicate vertical interlayer distances. (b) Induced-doping schematic diagram of G/CrP/G. (c) Electronic band structure and DOS. Blue shows the band projected onto two layers of graphene, which completely overlap; gray shows the band projected onto CrP in the band structure and total density of state. (d) Charge-density difference with an isovalue of 0.0003 e/Å^3. Yellow and blue regions indicate accumulation and depletion of electrons, respectively.

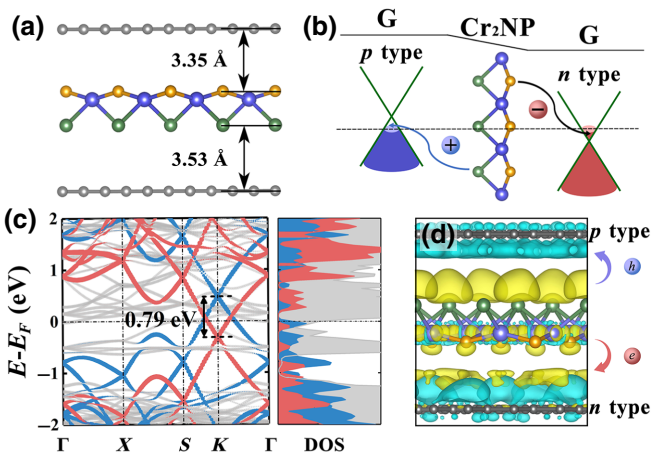

FIG. 6. (a) Structure of vdW heterostructure G/Cr_2NP/G. Numbers indicate vertical interlayer distances. (b) Induced-doping schematic diagram of G/Cr_2NP/G. (c) Electronic band structure and DOS. Red (blue) shows the band projected onto the graphene layer on the side of N (P) atoms; gray shows the band projected onto Cr_2NP in the band structure and total density of state. (d) Charge-density difference with an isovalue of 0.0003 e/Å^3. Yellow and blue regions indicate accumulation and depletion of electrons, respectively.

respectively. Similar to the CrP and CrAs monolayers, the Cr_2XY monolayers are also indirect semiconductors with band gaps ranging from 0.140 to 0.607 eV (middle part in Fig. 4). However, because the charges more dramatically transfer from Cr to N atoms after N atomic substitution, significantly affecting the electronic structure, the situations are completely different in Cr_2NY monolayers (lower part in Fig. 4). First, Cr_2NP retains an indirect gap with CBM and VBM edges residing at the S and Γ points, while Cr_2NAs becomes a direct-gap semiconductor with the CBM and VBM edges both located at the S point. The energy gaps of Cr_2NP and Cr_2NAs are 0.818 and 0.872 eV, respectively, which are much bigger than those of CrY and Cr_2XY. Things are more interesting in Cr_2NSb for which the CBM and VBM edges meet at the S point, leading to a very small energy gap close to 0 eV, and both the CBM and VBM come from spin-up bands, indicating that the Cr_2NSb monolayer is a 2D spin-gapless semiconductor (SGS) [53–55]. The electron-excitation behavior with only spin-up carriers in the SGS can always easily happen, suggesting that the Cr_2NSb monolayer has potential applications in spintronics.

B. The *p*-*n* vertical junctions induced by symmetry breaking

The special structures of Cr_2NY monolayers result in a large dipole, especially for Cr_2NP. To explore their applications, we use CrP and Cr_2NP as an intermediate layer sandwiched between two layers of graphene (G), forming vdW heterostructures G/CrP/G [Fig. 5(a)] and G/Cr_2NP/G [Fig. 6(a)], respectively. Here, to minimize the lattice mismatch between CrP (Cr_2NP) and graphene layers, we consider $\sqrt{5}\times\sqrt{5}\times 1$ and $\sqrt{15}\times\sqrt{15}\times 1$ supercells of CrP (Cr_2NP) and graphene, respectively. All the atomic positions and lattice vectors of the heterostructures are fully relaxed, and we obtain a vertical interlayer distance of 3.43 Å for G/CrP/G, with no chemical bonds at the interface region, indicating the existence of a weak vdW interaction. For the G/Cr_2NP//G heterostructure, the vdW interaction between Cr_2NP and graphene is stronger (weaker) at the N- (P-) atom side because of the shorter (longer) layer distance of 3.35 Å (3.53 Å). The energetic stability is examined by the bonding energy, E_b, comparing the total energies of the final heterostructure with those of the isolated components:

$$E_b = E_H - E_{\rm in} - E_{\rm G1} - E_{\rm G2},$$

where E_H, $E_{\rm in}$, $E_{\rm G1}$, and $E_{\rm G2}$ are the energies of the heterostructure, isolated intermediate layer, and graphene on two sides. It is found that the formation of G/CrP/G (G/Cr_2NP/G) is an exothermic process with E_b of -2.29 eV (-2.36 eV), indicating the energetic stability.

Figure 5(b) shows induced p-type doping of two graphene sheets in G/CrP/G, because the Dirac points of graphene have the same energy and both are higher than the Fermi level from the electronic bands and density of states (DOS) projected onto the graphene layers [Fig. 5(c)]. Moreover, the interfacial interaction is analyzed by charge-density difference, as shown in Fig. 5(d), where the carriers

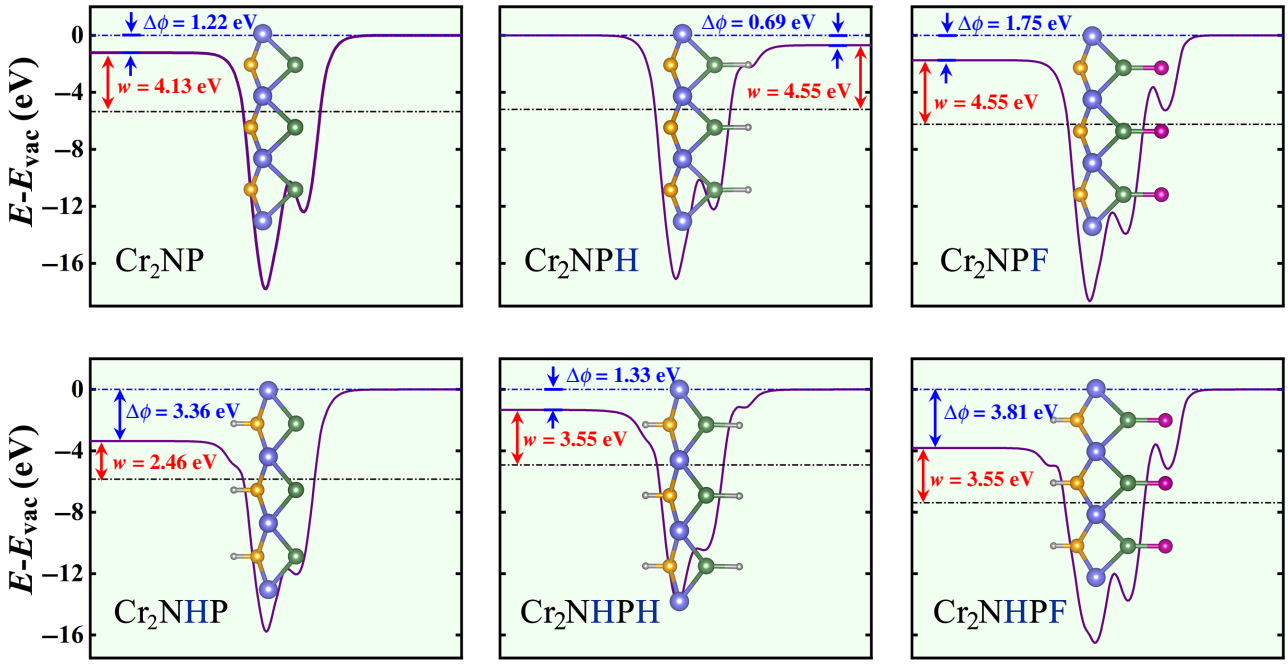

FIG. 7. Electrostatic potential of functionalized Cr_2NP in the direction perpendicular to the layers. Electrostatic potential differences ($\Delta\phi$) between two sides are indicated by blue arrows; work functions (w) of the side with lower potential are shown by red arrows.

from CrP to two graphene sheets are holes, further proving the same p-type doping of the graphene sheets. For the G/Cr_2NP/G case, due to the intrinsic dipole of Janus Cr_2NP, different doping types are induced in the two graphene sheets [Fig. 6(b)]. In Fig. 6(c), red (blue) shows the band or DOS projected onto the graphene sheet on the N (P) side, which displays n-type (p-type) doping for graphene with the Dirac point being lower (higher) than the Fermi level. The Dirac point difference of 0.79 eV can be used to describe the difference in doping between the two graphene sheets. This phenomenon is derived from the interfacial interaction between graphene and Janus Cr_2NP. From the charge-density difference, as shown in Fig. 6(d), because of the built-in vertical electric field generated from the dipole of the Cr_2NP monolayer, the electrons (holes) can be transferred from the intermediate layer to the graphene sheets by the N (P) side, forming n-type (p-type) doping of graphene. Therefore, an ultrathin p-n vertical junction is naturally formed [56,57], indicating that symmetry breaking is an effective strategy to make such 2D materials exciting and useful in nanoelectronics.

The strategy of functionalization can further break symmetry and have an impact on the properties of 2D materials [58,59]. We next consider that hydrogenating and fluorinating at N(Cr_2NHP or Cr_2NFP) or P(Cr_2NPH or Cr_2NPF) atoms to tune the electronic properties, which are stable composite structures, except for the Cr_2NFP monolayer. The Bader charges and dipole moments are calculated and listed in Table SIII within the Supplemental Material [47]. It is found that the electrons transfer from P to F atoms in the Cr_2NPF monolayer, because the electronegativity of the F atom is greater than that of the P atom, and the electrons transfer from P to H atoms in Cr_2NPH and from H to N atoms in the Cr_2NHP monolayer, due to the electronegativity of the H atom being greater than that of the P atom but smaller than the N atom. Interestingly, the dipole moments are enhanced in Cr_2NHP and Cr_2NPF monolayers, but decrease and are even converted to the opposite direction for the Cr_2NPH monolayer. Affected by the changes to the dipole, the electrostatic potential differences shown in Fig. 7 become larger in Cr_2NPF and Cr_2NHP, but become negative in Cr_2NPH, which is consistent with the previous conclusion for Janus Cr_2XY and Cr_2NY. Moreover, an interesting result for the Cr_2NHP monolayer is that hydrogenating it can lower its work function to 2.46 eV. At the surface of photoelectric devices, the capture and excitation of charge are essential and a lower work function can make them easily achieved, indicating that the Cr_2NHP monolayer is a potential electron-emission-layer material.

We also consider that functionalization on both sides of the Cr_2NP monolayer, including for Cr_2NHPH and Cr_2NHPF, which can be viewed as functionalization at the P atom in Cr_2NHP. As listed in Table SIII within the Supplemental Material [47], the dipole moment is weakened when hydrogenating and enhanced when fluorinating, compared with Cr_2NHP, and the electrostatic potential differences (Fig. 7) increase or decrease accordingly. Thus, a large dipole moment of up to 1.53 D is obtained for the Cr_2NHPF monolayer. A $\sqrt{5} \times \sqrt{5} \times 1$ supercell of

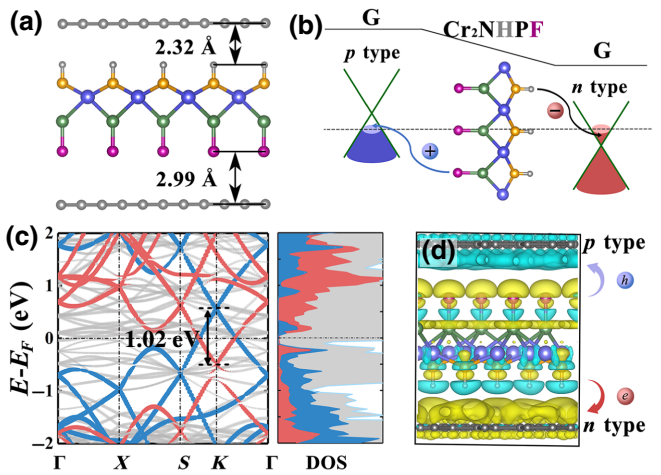

FIG. 8. (a) Structure of vdW heterostructure G/Cr_2NHPF/G. Numbers indicate vertical interlayer distances. (b) Induced-doping schematic diagram of G/Cr_2NHPF/G. (c) Electronic band structure and DOS. Red (blue) shows the band projected onto the graphene layer on the side of H (F) atoms; gray shows the band projected onto Cr_2NP in the band structure and total density of state. (d) Charge-density difference with an isovalue of 0.0003 e/Å^3. Yellow and blue regions indicate accumulation and depletion of electrons, respectively.

Cr_2NHPF is sandwiched between two graphene sheets, forming vdW heterostructures G/Cr_2NHPF/G [Fig. 8(a)], where layer distances are shorter on both sides compared with G/Cr_2NP/G, indicating a stronger interfacial interaction. The E_b of -2.36 eV can further prove its energetic stability. Like the G/Cr_2NF/G case, the induced doping principle of G/Cr_2NHPF/G depicted in Fig. 8(b) is the same. As expected, as shown in Fig. 8(c), more obvious doping can be found in graphene sheets of G/Cr_2NHPF/G with the Dirac point difference increasing to 1.02 eV because of the larger vertical electric field. The stronger interfacial interaction can be confirmed by the charge-density difference [Fig. 8(d)], where the carrier transfers from Cr_2NHPF to graphene on the fluorinated P atom (hydrogenated N atom) side is net electrons (holes). Therefore, based on G/Cr_2NHPF/G, an ultrathin p-n vertical junction with a larger carrier concentration can potentially be prepared; this has great potential for application in nanoelectronics.

C. Hydrogen-evolution reaction performance induced by symmetry breaking

We finally investigate the symmetry-breaking-induced hydrogen-evolution reaction (HER) performance of 2D Cr-based materials. The electrocatalytic activities for the HER are investigated in a $2 \times 2 \times 1$ supercell of the monolayers by calculating the Gibbs free energy (ΔG). The Sabatier principle states that the interaction between the catalyst and H atoms should be neither too strong nor too weak [60,61]. Here, we find that the ΔG has large positive values (Fig. S5 within the Supplemental Material [47]) for P-, As-, and Sb-atom sites in CrY and Cr_2XY monolayers, indicating that the interaction between the monolayers and H atom is weak, and the desorption reaction can more easily happen, but the adsorption reaction would be restricted. On the contrary, the N-atom sites in Cr_2NY monolayers display excellent HER activities. As shown in Fig. 9(a), ΔG has small values of 0.155, 0.049, and 0.024 eV for the N-atom sites in Cr_2NP, Cr_2NAs, and Cr_2NSb monolayers, respectively, indicating their good catalytic activity, which is even better than that of Pt ($|\Delta G| = 0.09$ eV) for Cr_2NAs and Cr_2NSb. Interestingly, we note that the HER catalytic activity mainly depends on the electronegativity of the adsorption sites: ΔG has smaller values at sites with higher electronegativity. Thereby, P-, As-, and Sb-atom sites are catalytically inactive, while N-atom sites have better activities. On the other hand, it is not negligible for the atoms of nonadsorption sites: the adsorption sites have better activities when the nonadsorption sites possess lower electronegativity. Therefore, in Cr_2NY monolayers, the N-atom sites in the Cr_2NSb monolayer have the best HER performance due to the Sb atom having the lowest electronegativity.

To explore the mechanism of the HER activity difference in 2D Cr-based materials, Bader charges of adsorbing sites in slab monolayers are calculated and summarized in Fig. S5 within the Supplemental Material [47]. It is found that the adsorbing sites with higher electronegativity obtain more electrons, and the amount decreases (increases) with an increase (decrease) in the electronegativity of nonadsorption sites. The atom sites accumulating more charges have stronger interactions with the H atom, which means that more stable adsorbed states can be formed and the difficulty of the desorption reaction can be reduced. Thus, the N-atom sites obtaining more electrons have the best HER activity, and the Cr_2NSb monolayer is the optimal HER catalyst because the Sb atom, with the lowest electronegativity, can promote the accumulation of charges at the N-atom sites.

It is demonstrated that external strain is an effective strategy to tune the HER performance of catalysts [62–66]. We apply biaxial tensile strains along the plane of the CrY and Cr_2XY monolayers and find that P-atom sites become HER active. Figure 9(b) shows the ΔG change of P-atom sites as a function of applied biaxial strain, where the case of Pt is taken as a catalytic window highlighted in green. One can see that, when the tensile strain is from 3% to 5%, the HER activity of the P-atom sites can be tuned to the catalytic window, thereby possessing better HER activities than that of Pt. Moreover, the values of ΔG are close to zero at a tensile strain of about 4%, leading to optimal HER performances of P-atom sites in the CrY and Cr_2XY monolayers. Therefore, by breaking the structural symmetry via N-atom substitution, the Cr_2NY monolayers have excellent

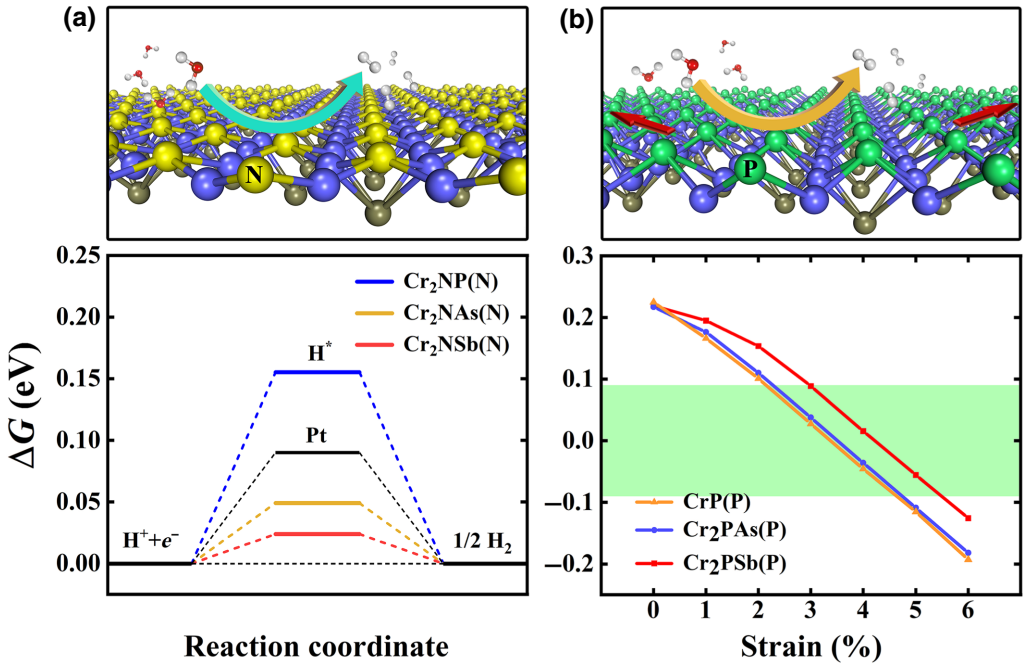

FIG. 9. Schematic diagram (top panels) and Gibbs free energies (lower panels) of a hydrogen atom adsorbed at (a) N sites of Cr_2NY monolayers and (b) P sites of structures with applied biaxial strain.

HER activity and by applying biaxial tensile strain, the 2D Cr-based materials become HER active.

IV. CONCLUSIONS

We propose a series of Janus Cr_2NY (Y = P, As, Sb) monolayers with multiple functionalities by breaking the structural symmetry of CrY. The results show that the geometric and electronic structures can be significantly regulated, which result in a larger dipole, and have great potential for various applications of Cr_2NY. Specifically, Cr_2NSb possesses a fascinating electronic band and is a spin-gapless semiconductor. Through the strategy of functionalization, further breaking the symmetry of Cr_2NP, the work function can be lowered to 2.46 eV and the dipole moment can be enhanced to 1.53 D. By sandwiching either Cr_2NP or functionalized Cr_2NP between two graphene sheets, the interfacial interaction will induce different types of carrier doping in the graphene sheets, generating an ultrathin p-n junction. Moreover, structural symmetry breaking can promote the accumulation of charges at the N sites of Cr_2NY, leading to optimal hydrogen-evolution performance, especially for Cr_2NSb. Through breaking symmetry, we rationally design multifunctional 2D Janus materials with exciting applications in nanoelectronics and clean energy conversion.

ACKNOWLEDGEMENTS

This work is supported by the National Natural Science Foundation of China (Grants No. 52172088 and No. 51772085) and the Natural Science Foundation of Hunan Province (No. 2020JJ4190 and No. 2021JJ30112).

[1] J. H. Park, A. Ndao, W. Cai, L. Hsu, A. Kodigala, T. Lepetit, Y. H. Lo, and B. Kante, Symmetry-breaking-induced plasmonic exceptional points and nanoscale sensing, Nat. Phys. **16**, 462 (2020).

[2] X. Zhang, Q. T. Cao, Z. Wang, Y. X. Liu, C. W. Qiu, L. Yang, Q. Gong, and Y. F. Xiao, Symmetry-breaking-induced nonlinear optics at a microcavity surface, Nat. Photonics **13**, 21 (2019).

[3] K. C. Shaing, Symmetry-Breaking Induced Transport in the Vicinity of a Magnetic Island, Phys. Rev. Lett. **87**, 245003 (2001).

[4] H. Guan, N. Tang, H. Huang, X. Zhang, M. Su, X. Liu, L. Liao, W. Ge, and B. Shen, Inversion symmetry breaking induced Valley Hall effect in multilayer WSe_2, ACS Nano **13**, 9325 (2019).

[5] J. Sung, Y. Zhou, G. Scuri, V. Zolyomi, T. I. Andersen, H. Yoo, D. S. Wild, A. Y. Joe, R. J. Gelly, H. Heo, S. J. Magorrian, D. Berube, A. M. M. Valdivia, T. Taniguchi, K. Watanabe, M. D. Lukin, P. Kim, V. I. Fal'ko, and H. Park, Broken mirror symmetry in excitonic response of reconstructed domains in twisted $MoSe_2/MoSe_2$ bilayers, Nat. Nanotechnol. **15**, 750 (2020).

[6] J. C. Lian, W. Q. Huang, W. Y. Hu, and G. F. Huang, Electrostatic potential anomaly in 2D Janus transition metal dichalcogenides, Ann. Phys. **531**, 1900369 (2019).

[7] A. Y. Lu, H. Zhu, J. Xiao, C. P. Chuu, Y. Han, M. H. Chiu, C. C. Cheng, C. W. Yang, K. H. Wei, Y. Yang, Y. Wang, D. Sokaras, D. Nordlund, P. Yang, D. A. Muller, M. Y. Chou,

X. Zhang, and L. J. Li, Janus monolayers of transition metal dichalcogenides, Nat. Nanotechnol. **12**, 744 (2017).

[8] J. Zhang, S. Jia, I. Kholmanov, L. Dong, D. Er, W. Chen, H. Guo, Z. Jin, V. B. Shenoy, L. Shi, and J. Lou, Janus monolayer transition-metal dichalcogenides, ACS Nano **11**, 8192 (2017).

[9] T. Zheng, Y. C. Lin, Y. Yu, P. Valencia Acuna, A. A. Puretzky, R. Torsi, C. Liu, I. N. Ivanov, G. Duscher, D. B. Geohegan, Z. Ni, K. Xiao, and H. Zhao, Excitonic dynamics in Janus MoSSe and WSSe monolayers, Nano Lett. **21**, 931 (2021).

[10] S. B. Yu, M. Zhou, D. Zhang, and K. Chang, Spin Hall effect in the monolayer Janus compound MoSSe enhanced by Rashba spin-orbit coupling, Phys. Rev. B **104**, 075435 (2021).

[11] X. Ma, X. Wu, H. Wang, and Y. Wang, A Janus MoSSe monolayer: A potential wide solar-spectrum water-splitting photocatalyst with a low carrier recombination rate, J. Mater. Chem. A **6**, 2295 (2018).

[12] S. Liu, J. N. Fry, and H. P. Cheng, Multiple control of few-layer Janus MoSSe systems, Phys. Rev. Mater. **5**, 064007 (2021).

[13] R. Peng, Y. Ma, S. Zhang, B. Huang, and Y. Dai, Valley polarization in Janus single-layer MoSSe via magnetic doping, J. Phys. Chem. Lett. **9**, 3612 (2018).

[14] C. Jin, X. Tang, X. Tan, S. C. Smith, Y. Dai, and L. Kou, A Janus MoSSe monolayer: A superior and strain-sensitive gas sensing material, J. Mater. Chem. A **7**, 1099 (2019).

[15] M. Idrees, H. U. Din, R. Ali, G. Rehman, T. Hussain, C. V. Nguyen, I. Ahmad, and B. Amin, Optoelectronic and solar cell applications of Janus monolayers and their van der Waals heterostructures, Phys. Chem. Chem. Phys. **21**, 18612 (2019).

[16] K. Liang, T. Huang, K. Yang, Y. Si, H. Y. Wu, J. C. Lian, W. Q. Huang, W. Y. Hu, and G. F. Huang, Dipole Engineering of Two-Dimensional van der Waals Heterostructures for Enhanced Power-Conversion Efficiency: The Case of Janus Ga_2SeTe/InS, Phys. Rev. Appl. **16**, 054043 (2021).

[17] D. Er, H. Ye, N. C. Frey, H. Kumar, J. Lou, and V. B. Shenoy, Prediction of enhanced catalytic activity for hydrogen evolution reaction in Janus transition metal dichalcogenides, Nano Lett. **18**, 3943 (2018).

[18] F. Ersan and C. Ataca, Janus PtX_nY2-_n (X, $Y = S$, Se, Te; $0 \le n \le 2$) Monolayers for Enhanced Photocatalytic Water Splitting, Phys. Rev. Appl. **13**, 064008 (2020).

[19] S. Zhang, Y. Li, T. Zhao, and Q. Wang, Robust ferromagnetism in monolayer chromium nitride, Sci. Rep. **4**, 5241 (2014).

[20] A. V. Kuklin, A. A. Kuzubov, E. A. Kovaleva, N. S. Mikhaleva, F. N. Tomilin, H. Lee, and P. V. Avramov, Two-dimensional hexagonal CrN with promising magnetic and optical properties: A theoretical prediction, Nanoscale **9**, 621 (2017).

[21] M. Modarresi, A. Mogulkoc, Y. Mogulkoc, and A. N. Rudenko, Lateral Spin Valve Based on the Two-Dimensional CrN/P/CrN Heterostructure, Phys. Rev. Appl. **11**, 064015 (2019).

[22] A. Mogulkoc, M. Modarresi, and A. N. Rudenko, Two-dimensional chromium pnictides CrX ($X = $P, As, sb): Half-metallic ferromagnets with high Curie temperature, Phys. Rev. B **102**, 024441 (2020).

[23] A. N. Ma, P. J. Wang, and C. W. Zhang, Intrinsic ferromagnetism with high temperature, strong anisotropy and controllable magnetization in the CrX ($X = $P, As monolayer, Nanoscale **12**, 5464 (2020).

[24] Z. H. Yang, J. H. Ren, T. Huang, W. Q. Huang, W. Y. Hu, and G. F. Huang, Two-dimensional chromium phosphorus monolayer based gas sensors to detect NO_x: A first-principles study, Results Phys. **32**, 105100 (2022).

[25] A. Mogulkoc, M. Modarresi, and A. N. Rudenko, Two-Dimensional Chromium Bismuthate: A Room-Temperature Ising Ferromagnet with Tunable Magneto-Optical Response, Phys. Rev. Appl. **15**, 064053 (2021).

[26] B. Huang, G. Clark, E. Navarro Moratalla, D. R. Klein, R. Cheng, K. L. Seyler, D. Zhong, E. Schmidgall, M. A. McGuire, D. H. Cobden, W. Yao, D. Xiao, P. Jarillo-Herrero, and X. Xu, Layer-dependent ferromagnetism in a van der Waals crystal down to the monolayer limit, Nature **546**, 270 (2017).

[27] B. Huang, G. Clark, D. R. Klein, D. MacNeill, E. Navarro Moratalla, K. L. Seyler, N. Wilson, M. A. McGuire, D. H. Cobden, D. Xiao, W. Yao, P. Jarillo-Herrero, and X. Xu, Electrical control of 2D magnetism in bilayer CrI_3, Nat. Nanotechnol. **13**, 544 (2018).

[28] S. Jiang, L. Li, Z. Wang, K. F. Mak, and J. Shan, Controlling magnetism in 2D CrI_3 by electrostatic doping, Nat. Nanotechnol. **13**, 549 (2018).

[29] Y. Hou, J. Kim, and R. Wu, Magnetizing topological surface states of Bi_2Se_3 with a CrI_3 monolayer, Sci. Adv. **5**, eaaw1874 (2019).

[30] S. I. Vishkayi, Z. Torbatian, A. Qaiumzadeh, and R. Asgari, Strain and electric-field control of spin-spin interactions in monolayer CrI_3, Phys. Rev. Mater. **4**, 094004 (2020).

[31] T. Olsen, Unified Treatment of Magnons and Excitons in Monolayer CrI_3 from Many-Body Perturbation Theory, Phys. Rev. Lett. **127**, 166402 (2021).

[32] L. Ren, Q. Liu, P. Xu, Z. Zhong, L. Yang, Z. Yuan, and K. Xia, Noncollinearity-Modulated Electronic Properties of Monolayer CrI_3, Phys. Rev. Appl. **11**, 054042 (2019).

[33] N. Sivadas, S. Okamoto, X. Xu, C. J. Fennie, and D. Xiao, Stacking-dependent magnetism in bilayer CrI_3, Nano Lett. **18**, 7658 (2018).

[34] J. Kim, K. W. Kim, B. Kim, C. J. Kang, D. Shin, S. H. Lee, B. C. Min, and N. Park, Exploitable magnetic anisotropy of the two-dimensional magnet CrI_3, Nano Lett. **20**, 929 (2020).

[35] G. Kresse and J. Furthmüller, Efficient iterative schemes for *ab initio* total-energy calculations using a plane-wave basis set, Phys. Rev. B **54**, 11169 (1996).

[36] G. Kresse and J. Hafner, *Ab initio* molecular-dynamics simulation of the liquid-metal–amorphous-semiconductor transition in germanium, Phys. Rev. B **49**, 14251 (1994).

[37] P. E. Blöchl, Projector augmented-wave method, Phys. Rev. B **50**, 17953 (1994).

[38] J. P. Perdew, K. Burke, and M. Ernzerhof, Generalized Gradient Approximation Made Simple, Phys. Rev. Lett. **77**, 3865 (1996).

[39] H. T. Jeng and G. Y. Guo, First-principles investigations of orbital magnetic moments and electronic structures

of the double perovskites Sr_2FeMoO_6, Sr_2FeReO_6, and Sr_2CrWO_6, Phys. Rev. B **67**, 094438 (2003).

[40] Q. Li, K. Q. Chen, and L. M. Tang, Large Valley Splitting in van der Waals Heterostructures with Type-III Band Alignment, Phys. Rev. Appl. **13**, 014064 (2020).

[41] J. Heyd, J. E. Peralta, G. E. Scuseria, and R. L. Martin, Energy band gaps and lattice parameters evaluated with the Heyd-Scuseria-Ernzerhof screened hybrid functional, J. Phys. Chem. C **123**, 174101 (2005).

[42] J. Heyd, G. E. Scuseria, and M. Ernzerhof, Hybrid functionals based on a screened Coulomb potential, J. Phys. Chem. C **118**, 8207 (2003).

[43] J. A. White and D. M. Bird, Implementation of gradient-corrected exchange-correlation potentials in Car-Parrinello total-energy calculations, Phys. Rev. B **50**, 4954 (1994).

[44] P. Giannozzi, S. De Gironcoli, P. Pavone, and S. Baroni, *Ab initio* calculation of phonon dispersions in semiconductors, Phys. Rev. B **43**, 7231 (1991).

[45] X. Gonze, J. C. Charlier, D. C. Allan, and M. P. Teter, Interatomic force constants from first principles: The case of α-quartz, Phys. Rev. B **50**, 13035 (1994).

[46] X. Gonze and C. Lee, Dynamical matrices, Born effective charges, dielectric permittivity tensors, and interatomic force constants from density-functional perturbation theory, Phys. Rev. B **55**, 10355 (1997).

[47] See the Supplemental Material at http://link.aps.org/supplemental/10.1103/PhysRevApplied.18.014013 for the calculated formation energies, formation enthalpies, elastic constants, phonon dispersion, Bader charges, atomic layer spacings, and local dipole moments of the CrY, Cr_2XY, and Cr_2NY monolayers; the phonon dispersion of CrN and the selected high-symmetry k path in the Brillouin zones; the AIMD simulations of Cr_2NP and Cr_2NAs; a comparison of the total and local dipole moments; the Gibbs free energies of adsorbing a hydrogen atom at different sites of the CrY, Cr_2XY, and Cr_2NY supercell; and the Bader charges and dipole moments of functionalized Cr_2NP.

[48] C. Xia, W. Xiong, J. Du, T. Wang, Y. Peng, and J. Li, Universality of electronic characteristics and photocatalyst applications in the two-dimensional Janus transition metal dichalcogenides, Phys. Rev. B **98**, 165424 (2018).

[49] Y. Mogulkoc, R. Caglayan, and Y. O. Ciftci, Band Alignment in Monolayer Boron Phosphide with Janus MoSSe Heterobilayers under Strain and Electric Field, Phys. Rev. Appl. **16**, 024001 (2021).

[50] B. Sun, Y. F. Ding, P. B. He, Y. Q. Zhao, and M. Q. Cai, Tuning the Band Alignment and Electronic Properties of GaSe/SnX_2 ($X = $S, Se) Two-Dimensional van der Waals Heterojunctions via an Electric Field, Phys. Rev. Appl. **16**, 044003 (2021).

[51] M. Sun and U. Schwingenschlögl, δ-CS: A Direct-Band-Gap Semiconductor Combining Auxeticity, Ferroelasticity, and Potential for High-Efficiency Solar Cells, Phys. Rev. Appl. **14**, 044015 (2020).

[52] Z. Li, J. Li, C. He, T. Ouyang, C. Zhang, S. Zhang, C. Tang, R. A. Römer, and J. Zhong, Few-Layer β-SnSe with Strong Visible Light Absorbance and Ultrahigh Carrier Mobility, Phys. Rev. Appl. **13**, 014042 (2020).

[53] X. L. Wang, Proposal for a New Class of Materials: Spin Gapless Semiconductors, Phys. Rev. Lett. **100**, 156404 (2008).

[54] Y. Pan and Z. Yang, Electronic structures and spin gapless semiconductors in BN nanoribbons with vacancies, Phys. Rev. B **82**, 195308 (2010).

[55] E. Şaşıoğlu, T. Aull, D. Kutschabsky, S. Blügel, and I. Mertig, Half-Metal–Spin-Gapless-Semiconductor Junctions as a Route to the Ideal Diode, Phys. Rev. Appl. **14**, 014082 (2020).

[56] J. E. Padilha, R. H. Miwa, A. J. R. Da Silva, and A. Fazzio, Two-dimensional van der Waals *p-n* junction of InSe/phosphorene, Phys. Rev. B **95**, 195143 (2017).

[57] M. Palsgaard, T. Gunst, T. Markussen, K. S. Thygesen, and M. Brandbyge, Stacked Janus device concepts: Abrupt *pn*-junctions and cross-plane channels, Nano Lett. **18**, 7275 (2018).

[58] A. Ugolotti, G. P. Brivio, and G. Fratesi, Coverage-dependent electronic and optical properties of H- or F-passivated Si/Ag(111) from first principles, Phys. Rev. B **101**, 195413 (2020).

[59] Z. Q. Huang, M. L. Xu, G. Macam, C. H. Hsu, and F. C. Chuang, Large-gap topological insulators in functionalized ordered double transition metal carbide MXenes, Phys. Rev. B **102**, 075306 (2020).

[60] B. R. Garrett, S. M. Polen, K. A. Click, M. He, Z. Huang, C. M. Hadad, and Y. Wu, Tunable molecular MoS_2 edge-site mimics for catalytic hydrogen production, Inorg. Chem. **55**, 3960 (2016).

[61] A. B. Laursen, A. S. Varela, F. Dionigi, H. Fanchiu, C. Miller, O. L. Trinhammer, J. Rossmeisl, and S. Dahl, Electrochemical hydrogen evolution: Sabatier's principle and the volcano plot, J. Chem. Educ. **89**, 1595 (2012).

[62] X. Wang, Y. Zhu, A. Vasileff, Y. Jiao, S. Chen, L. Song, B. Zheng, Y. Zheng, and S. Z. Qiao, Strain effect in bimetallic electrocatalysts in the hydrogen evolution reaction, ACS Energy Lett. **3**, 1198 (2018).

[63] S. Liu, Z. Hu, Y. Wu, J. Zhang, Y. Zhang, B. Cui, C. Liu, S. Hu, N. Zhao, X. Han, A. Cao, Y. Chen, Y. Deng, and W. Hu, Dislocation-strained IrNi alloy nanoparticles driven by thermal shock for the hydrogen evolution reaction, Adv. Mater. **32**, 2006034 (2020).

[64] K. Yan, T. A. Maark, A. Khorshidi, V. A. Sethuraman, A. A. Peterson, and P. R. Guduru, The influence of elastic strain on catalytic activity in the hydrogen evolution reaction, Angew. Chem., Int. Ed. **55**, 6175 (2016).

[65] T. Huang, Y. Si, H. Y. Wu, L. X. Xia, Y. Lan, W. Q. Huang, W. Y. Hu, and G. F. Huang, Strain and interfacial engineering to accelerate hydrogen evolution reaction of two-dimensional phosphorus carbide, Chin. Phys. B **30**, 027101 (2021).

[66] A. Alinezhad, L. Gloag, T. M. Benedetti, S. Cheong, R. F. Webster, M. Roelsgaard, B. B. Iversen, W. Schuhmann, J. J. Gooding, and R. D. Tilley, Direct growth of highly strained Pt islands on branched Ni nanoparticles for improved hydrogen evolution reaction activity, J. Am. Chem. Soc. **141**, 16202 (2019).